(Received 6 June 2025, Accepted 20 August 2025, Scheduled 5 September 2025)

Magnetic Density Analysis and Performance Optimization of Hybrid Excitation Starter Generator

Hui Zhu[1], Wenjing Hu[2,*], Wei Wang[3], Shiqiang Liu[2], Xia Zhang[4], Jiewen Li[5], and Xingxu Jin[2]

[1] School of Engineering, Shandong Union University, China
[2] School of Transportation and Vehicle Engineering, Shandong University of Technology, China
[3] China National Heavy Duty Truck Group Co., Ltd., China
[4] Zibo Yongtai Motor Co., Ltd., China
[5] Weifang Petri Electric Co., Ltd., China

ABSTRACT: Hybrid excitation starter generator (HESG) has an increased number of magnetic potential sources, leading to issues such as complex magnetic circuits, numerous structural parameters, and low space utilization. These factors cause traditional analysis methods to have long cycles and low accuracy. In this paper, a new type of salient pole electromagnetic and permanent magnet composite pole HESG is proposed, and an analysis method combining hierarchical optimization and Taguchi method to analyze the influence of different structural parameters of composite pole rotor on the HESG performance is proposed. Response surface method was used to simulate the stator groove with multiple objectives, analyze the electromagnetic characteristics of HESG, complete the performance optimization, prototype, and conduct experiments. The results show that the amplitude of the air gap magnetic density base of HESG is increased by 7.4%; the distortion rate is reduced by 10.6%; the output voltage is increased to 127.68 V; the output performance and magnetization ability are significantly improved; and the overall performance of the HESG is improved.

1. INTRODUCTION

In an automobile power system, power generation system is an important component, and its output performance and output quality determine the safety of the automobile battery and electrical equipment. Permanent magnet synchronous motor (PMSM) has become a research hotspot because of its advantages of small size, high efficiency, large torque, and wide speed regulation range, but PMSM also has the disadvantages of constant magnetic field and high copper consumption of the straight-axis armature current during weak magnetization [1]. HESG integrates permanent magnet and electric excitation sources, inheriting the high power density of permanent magnet synchronous starter generators and the adjustable air-gap magnetic field of electric excitation synchronous starter generators. It overcomes the shortcomings of both types, meeting the needs of electric vehicle range extenders and starter engines. However, its diverse topology and complex magnetic circuit composition complicate magnetic field analysis [2–6]. Effective magnetic field analysis is one of the important means to optimize the electromagnetic performance of generator and improve the output quality, which is of great significance for the design and optimization of high-performance HESGs. Therefore, the study of more reasonable topologies and more accurate magnetic field analysis methods has become a key research direction to improve the performance of HESGs.

The hybrid excitation structure is categorized into series HESG, parallel HESG, and series-parallel HESG according to the relationship between permanent magnet magnetic potential and electric excitation magnetic potential [7]. In recent years, scholars have been innovating hybrid excitation topology, and a variety of HESG structures have appeared. Ref. [8] proposes a two-rotor hybrid excitation axial flux switching topology, which has the advantages of high power/torque density and high torque at low speeds. However, this structure features a double-rotor design with a double-layer air gap, resulting in a larger equivalent air gap length. Consequently, the number of permanent magnets used increases under the same performance requirements, leading to relatively higher costs. Ref. [9] proposes a hybrid excitation topology based on an electromagnetic claw pole structure, which improves efficiency by placing permanent magnets between the claw poles. However, the centrifugal force generated by this structure can easily cause the permanent magnets to dislodge during high-speed operation, so the placement of permanent magnets needs to be specially handled. Ref. [10] proposes a hybrid excitation structure composed of permanent magnet poles and electromagnet poles, in which a set of electric excitation windings is added to the permanent magnet, serving both as a backup winding to prevent internal faults and as a winding specifically for weakening the permanent magnet poles. However, the presence of two sets of electric excitation windings in this structure not only complicates control but also results in the second set of windings occupying winding space and reducing spatial utilization. Refs. [11–13] propose a hybrid excitation topology for rotor magnetic splitting, which utilizes a modular structure to significantly reduce

* Corresponding author: Wenjing Hu (huwenjing@sdut.edu.cn).

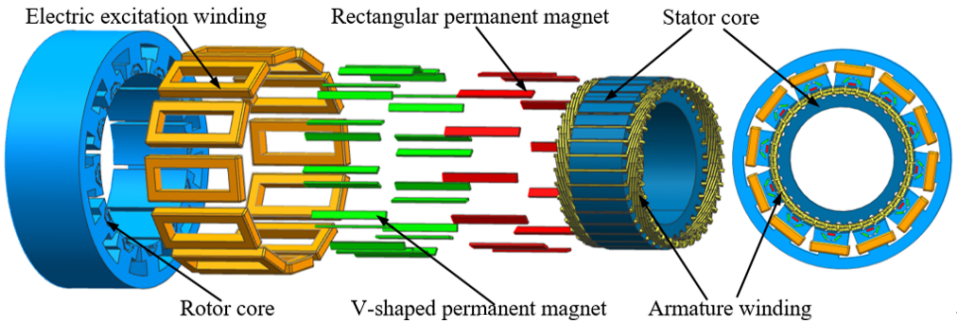

FIGURE 1. Structure of HESG.

TABLE 1. The table of main structure parameters.

Parameter	Value	Parameter	Value
Power rating/kW	1.5/2.0	Stator outer diameter/mm	200
Rated speed/(r· min^{1})/mm	200/4000	Air gap length/mm	0.5
Rotor outer diameter/mm	271	Axial length/mm	55

the eddy current losses of solid magnetic poles and permanent magnets. However, the addition of a magnetic conductivity bridge introduces an extra air gap, increases new leakage flux, and raises the magnetic resistance of the rotor magnetic shunt, resulting in reduced power density. Ref. [14] presents a segmented rotor hybrid excitation topology, where two windings are arranged in a non-overlapping manner, effectively reducing both the copper cost and the length of the magnetic circuit. However, the excitation winding occupies the space intended for armature winding, which affects the power density and efficiency of the structure. A novel hybrid excitation topology is proposed in [15], in which the starter generator has a simple electric excitation magnetic circuit and a permanent magnet magnetic circuit that forms a parallel magnetic circuit, making it not easy to demagnetize. However, the space utilization and power density are relatively low, and the magnetic field regulation capability is inadequate. Ref. [16] studies a hybrid excitation topology with variable magnetic poles, which alters the number of poles of the rotor by changing the polarity and amplitude of the electric excitation to vary the rotational speed, allowing for a wide range of rotational speeds. However, in this structure, the electric excitation and permanent magnets are in series, resulting in a larger current flowing through the electric excitation, higher copper losses in the excitation winding, and significant demagnetization of the permanent magnet. Scholars in [17] propose a new hybrid excitation topology structure with magnetic barriers and magnetic bridges, which features magnetic barriers opened at the bottom between adjacent permanent magnets to reduce magnetic leakage. A flux bridge is added in the middle of the rotor, and the magnetic field generated by the excitation winding is combined with the permanent magnetic field in the air gap through the stator core, forming a parallel magnetic circuit that reduces the likelihood of permanent magnet demagnetization. This topology has high power density, high efficiency, and certain magnetization capabilities. However, the flux bridge portion of the rotor is difficult to secure, and the spatial efficiency is relatively low.

Based on the above analysis, the current hybrid excitation topology is dominated by permanent magnet sources, so as to improve the power density, and the adjustment of the air-gap magnetic field is realized by increasing the electric excitation winding. However, there are still problems such as complex topology structure and large number of parameter components. In order to solve the above problems, this paper proposes an HESG with convex-pole electromagnetic and permanent magnet composite poles, and optimizes the rotor topology by using optimization analysis method combining hierarchical optimization and Taguchi method. This method fully considers the complex topological parameters of HESG, improves the accuracy of magnetic field analysis, and quickly determines the main influencing parameters of magnetic field, reducing the workload of finite element analysis. Using this method, the proposed air-gap magnetic field analysis model of HESG is derived; the main influencing parameters are analyzed; and the parameter optimization matching and electromagnetic performance analysis are completed.

2. HESG MAGNETIC FIELD ANALYSIS

The HESG is a 3-phase 12-pole 45-slot starter generator. The rated voltage is 72 V, rated speed 200 r/min, rated power 1500 W in starting mode, rated voltage 28 V, rated speed 4000 r/min, and rated power 2000 W in generating mode. Among them, the permanent magnet is made of neodymium iron boron material (NdFe35), and the stator core and rotor core are made of silicon steel sheets (DW315-50). The structure of the designed HESG is shown in Figure 1, and the main structural parameters are shown in Table 1.

The convex pole rotor structure is a “T” type structure, and the electro-excitation winding is wound on the pole body with

equal number of turns and opposite winding directions. The poles adjacent to the electro-excitation winding produce opposite polarity after the electro-excitation winding is energized. The permanent magnets of "V"+"—" structure are placed in the inner side of the convex rotor core near the center of the outer surface, and consist of 3 rectangular permanent magnets, which can not only improve the main air gap flux of each pole, but also improve the sinusoidal nature of the air gap magnetic density waveform, so as to make the starter generator have a larger output torque and higher power. The "T" type convex pole rotor structure combines the permanent magnet with the electric excitation winding, and the magnetic bridge provides the main magnetic flux path for electric excitation, which has small magnetoresistance and a wide range of regulation of induced electromotive force, so that the starter generator has a wide range of magnetization regulation. The polarity of the permanent magnets on the same side of the magnetic poles in the core of the same convex rotor is the same, and the magnetic poles of the core of the adjacent convex rotor are arranged adjacent to each other and at intervals under the action of the permanent magnets of the "V"+"—" structure. In order to verify the electromagnetic performance advantages of the designed structure, a simulation model is established, and the magnetic field lines, magnetic dense cloud diagram, and magnetic dense vector diagram are shown in Figure 2.

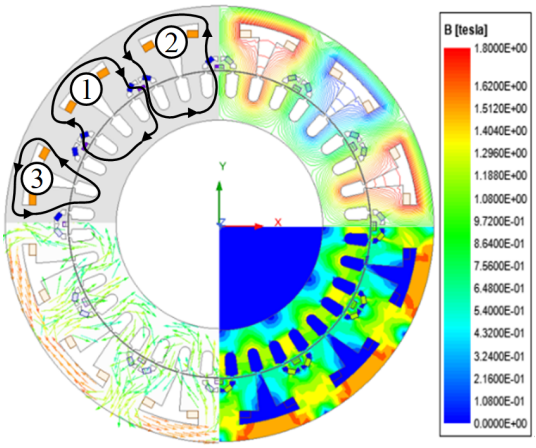

FIGURE 2. Finite element simulation 2D model diagram.

Figure 2 shows that there are three main magnetic flux paths, which are the main magnetic flux magnetic circuit 1 that passes through the "V" shape and "—" shape permanent magnet steel at the same time, the main magnetic flux magnetic circuit 2 that only passes through the "V" shaped permanent magnet steel, and the main magnetic flux magnetic circuit 3 that does not pass through the "V" shape and "—" shaped permanent magnet steel. The permanent magnetic field of the rotor is mainly distributed in the middle of the rotor poles, which results in a sparse distribution of magnetic field lines. Due to the addition of the excitation winding, the magnetic flux of the center of the designed rotor pole is ensured, and the shortcomings of the sparse magnetic field lines on both sides of the pole are compensated, and the magnetic field distribution of the designed rotor from the center of the pole to both sides is more uniform.

3. HESG ELECTROMAGNETIC ANALYSIS AND PARAMETER OPTIMIZATION

In order to ensure the good performance of the convex electromagnetic and permanent magnet compode HESG, the relevant structural size of the outer rotor of the starter generator was optimized by layering optimization and Taguchi method, so as to improve the air gap magnetic density of the starter generator as the optimization goal. The finite element simulation software was used to analyze and optimize the influence of rotor size on the air gap magnetic density, and the optimal rotor structure parameters were obtained. The schematic diagram of the rotor related parameters is shown in Figure 3.

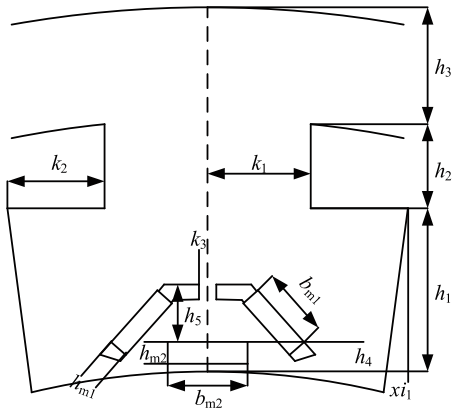

FIGURE 3. Schematic diagram of rotor-related parameters.

3.1. Influence of Different Rotor Parameters on Starter Generator Performance and Optimization

The air gap flux density $B_{\delta av}$ is expressed as:

$$B_{\delta av} = \frac{\Phi}{A_\delta} = \frac{\Phi_u}{\tau_P l_{ef}} \tag{1}$$

where Φ is the air gap flux per pole; Φ_u is the effective air gap flux; A_δ is the air gap cross-sectional area per pole; τ_P is the pole distance.

$$\begin{cases} \Phi_u^{'} + \Phi_{s2} = k\Phi_{m2} \\ kF_2 = \frac{k\Phi_{m2}}{G_{e2}} + \frac{\Phi_{s2}}{G_{s2}} \\ F_3 + \frac{2\Phi_{s2}}{G_{s2}} = \frac{(k\Phi_{m2} - \Phi_{s2})}{G_s} \\ +\Phi_u^{'}\left(\frac{3}{G_s} + \frac{1}{G_{e3}} + \frac{2}{G_r} + \frac{1}{G_y}\right) + F_d^{'} \end{cases} \tag{2}$$

$$\begin{cases} \Phi_u^{''} = (1-k)\,\Phi_{m2} - \Phi_{s2}^{'} + \Phi_{m1} - \Phi_{s1} \\ F_1 = \frac{\Phi_{m1}}{G_{e1}} + \frac{\Phi_{s1}}{G_{s1}} \\ (1-k)\,F_2 = \frac{(1-k)\Phi_{m2}}{G_{e2}} + \frac{\Phi_{s2}^{'}}{G_{s2}^{'}} \\ F_1 = \frac{\Phi_{m1}}{G_{e1}} + \Phi_u^{''}\left(\frac{2}{G_r} + \frac{1}{G_y}\right) + \frac{2(\Phi_{m1} - \Phi_{s1})}{G_s} + F_d^{''} \\ 2\,(1-k)\,F_2 = \frac{2(1-k)\Phi_{m2}}{G_{e2}} + \frac{\left[(1-k)\Phi_{m2} - \Phi_{s2}^{'}\right]}{G_s} \\ +\Phi_u^{''}\left(\frac{2}{G_s} + \frac{2}{G_r} + \frac{1}{G_y}\right) + F_d^{''} \end{cases} \tag{3}$$

Since the component of the armature reaction at no load of the starter generator $F_d^{'} = F_d^{''} = 0$, the above system of equations can be solved to obtain the following Equation (4).

$$\begin{cases} \Phi_{m2} = \frac{\{kF_2[(C_1G_sG_{s2}+2G_s+4G_{s2})G_{e3}+G_sG_{s2}]-F_3G_{e3}G_s\}G_{e2}}{(G_{e2}+G_{s2})[G_{e3}(C_1G_s+4)+G_s+G_{e2}]+2G_{e2}G_s} \\ \Phi_{s2} = \frac{\{kF_2G_{e2}[(C_1G_s+4)G_{e3}+G_s]-F_3G_{e3}G_s\}G_{s2}}{(G_{e2}+G_{s2})[G_{e3}(C_1G_s+4)+G_s+G_{e2}]+2G_{e2}G_s} \\ \Phi_u^{'} = \frac{[2kF_2G_{e2}+F_3(G_{e2}+G_{s2})]G_{e3}G_s}{(G_{e2}+G_{s2})[G_{e3}(C_1G_s+4)+G_s+G_{e2}]+2G_{e2}G_s} \end{cases} \tag{4}$$

where $C_1 = \frac{2}{G_r} + \frac{1}{G_y}$, where G_r is the rotor core permeability, and G_y is the stator core permeability.

No-load leakage coefficient σ_p:

$$\sigma_p = \frac{\Phi_m}{\Phi_u} = \frac{\Phi_{m1} + 2\Phi_{m2} + \Phi_{m3}}{\Phi_u^{'} + \Phi_u^{''}} \tag{5}$$

where Φ_m is the total magnetic flux produced by the starter generator electric excitation windings and permanent magnets.

The effective magnetic flux through the air gap Φ_u is:

$$\begin{aligned} \Phi_u = & \frac{[2kF_2G_{e2} + F_3(G_{e2}+G_{s2})]G_{e3}G_s}{(G_{e2}+G_{s2})[G_{e3}(C_1G_s+4)+G_s+G_{e2}]+2G_{e2}G_s} \\ & + \frac{\begin{array}{c} F_2(1-k)G_{e2}G_s(G_s+2G_{e1}+2G_{s1}^{'}) \\ +F_1G_{e2}G_s(G_{e1}+G_s+G_{s2}^{'}) \end{array}}{\begin{array}{c} G_s(G_{e1}+G_{s1})[(G_{e2}+G_{s2}^{'})(C_1+2C_2+2)+1] \\ +G_s^2[C_1(G_{e1}+G_{s1})+C_2(G_{e2}+G_{s2}^{'})+1] \end{array}} \end{aligned} \tag{6}$$

where F_1 is the equivalent magnetic potential of the electro-excitation winding, $F_1 = n'I$; G_{e1} is the equivalent internal permeability of the electro-excitation winding; its magnetoresistance is negligible.

Since the equivalent internal reluctance of the electro-excitation winding is negligible, G_{e1} is considered to tend to infinity. Equation (6) can be simplified as:

$$\begin{aligned} & \lim_{G_{e1}\to\infty} \Phi_u \\ & = \frac{[2kF_2G_{e2} + F_3(G_{e2}+G_{s2})]G_{e3}G_s}{(G_{e2}+G_{s2})[G_{e3}(C_1G_s+4)+G_s+G_{e2}]+2G_{e2}G_s} \\ & + \frac{(F_2(1-k)+n'I)G_{e2}}{[(G_{e2}+G_{s2}^{'})(C_1+2C_2+2)+1]+G_sC_1} \end{aligned} \tag{7}$$

To wit:

$$B_{\delta av} = \frac{1}{\tau_P l_{ef}} \left\{ \begin{array}{c} \frac{[2kF_2G_{e2}+F_3(G_{e2}+G_{s2})]G_{e3}G_s}{(G_{e2}+G_{s2})[G_{e3}(C_1G_s+4)+G_s+G_{e2}]+2G_{e2}G_s} \\ +\frac{(F_2(1-k)+n'I)G_{e2}}{[(G_{e2}+G_{s2}^{'})(C_1+2C_2+2)+1]+G_sC_1} \end{array} \right\} \tag{8}$$

where F_2 is the effective magnetic flux through the air gap "V" type permanent magnet equivalent magnetic potential, $F_2 = H_ch_{m1}$; G_{e2} is the "V" type magnetic field permanent magnet equivalent internal permeability, $G_{e2} = \mu_1\frac{S_{m1}}{h_{m1}}$, where μ_1 is the permeability of the permanent magnet, $\mu_1 = \mu_{r1}\mu_0 = \frac{B_r}{H_c}$ where μ_0 is the vacuum permeability, μ_{r1} the relative permeability of the permanent magnet material, and B_r the residual magnetic induction of the permanent magnet; S_{m1} is the axial cross-section of the permanent magnet, $S_{m1} = l_{m1}b_{m1}$; F_3 is the equivalent magnetic dynamic potential of a "I" permanent magnet, $F_3 = H_ch_{m2}$; G_{e3} is equivalent internal permeability of the "one" permanent magnet, $G_{e3} = \mu_1\frac{S_{m2}}{h_{m2}}$, where S_{m2} is the axial cross section of the "one" permanent magnet, $S_{m2} = l_{m2}b_{m2}$.

According to the formula, the effective magnetic flux of the air gap is mainly related to the magneto kinetic potential, the equivalent internal permeability of the permanent magnet, the air gap permeability, the stator and rotor core permeability, and the leakage permeability at the lower end of the "V" permanent magnet. The permanent magnet steel used in vehicle generators is mostly NdFe35 permanent magnet steel, and the number of turns of the electric excitation winding and the excitation current are part of the design parameters of the electric excitation magnetic field, which are determined by the power distribution of the generator. Excluding the main technical index parameters, the optimal improvement parameters of the main air gap magnetic field of the hybrid excitation generator can be obtained as the length of the permanent magnet, the length of the magnetization direction of the permanent magnet, the length of the effective air gap, and the basic size of the starter generator.

The air gap magneto magnetism is an intrinsic characteristic of the starter generator, which cannot directly characterize the performance of the starter generator, so the output torque and torque pulsation of the starter generator are added as references to analyze the influence of the rotor parameters on the performance of the starter generator. The finite element simulation of each rotor parameter is carried out to obtain the percentage diagrams of the influence of different parameters on the base wave amplitude of the air gap magnetic density, air gap magnetic density waveform distortion rate, the output torque of the starter generator, and the torque pulsation of the starter generator, as shown in Figures 4 and 5.

Parameters affecting four indicators (all over 4%) are b_{m1}, k_1, k_2; affecting three indicators are h_5, b_{m2}; affecting two are k_3, x_{i1}, h_1; affecting only a single indicator is h_3 (air gap magnetization) and h_{m1} (output torque); h_{m2}, h_2, h_4 have no significant effect. In order to ensure the magnetic field strength as well as reduce the loss, the permanent magnet magnetization thickness h_{m2} is taken as 3 mm, h_2 taken as 11 mm, and h_4 taken as 1.5 mm.

The finite element parametric analysis of h_3, with h_3 changing in the air gap magnetically dense average fundamental wave amplitude change curve is shown in Figure 6. As can be seen from Figure 6, with the increase of h_3, the average base wave amplitude of the air gap magnetization also increases. When h_3 is larger than 15 mm, the growth rate of the base wave amplitude slows down. The starter generator can obtain a stronger magnetic field strength when $h_3 = 15$ mm, thus $h_3 = 15$ mm is selected.

When $h_3 = 15$ mm, the finite element analysis of h_{m1} yields the curve of output torque as shown in Figure 7. From Figure 7, it can be seen that the output torque increases approximately linearly with the increase of h_{m1} before $h_{m1} = 5$ mm, and the slope of the increase of output torque slows down when h_{m1} is

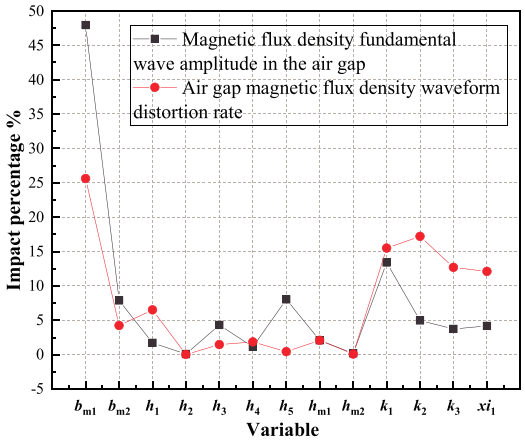

FIGURE 4. The proportion chart of the influence of different parameters on the average fundamental wave amplitude and the average distortion rate of the waveform in the air gap magnetic density.

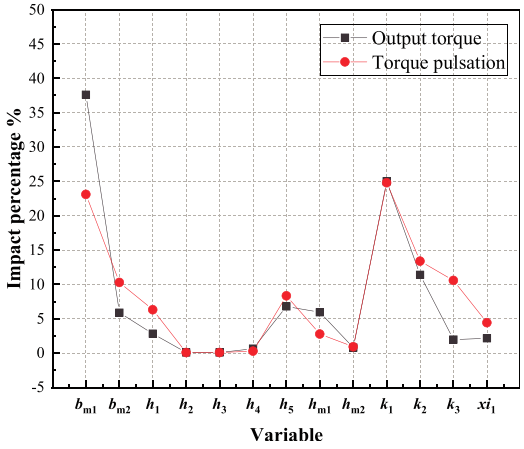

FIGURE 5. The proportion chart of the influence of different parameters on output torque and torque pulsation.

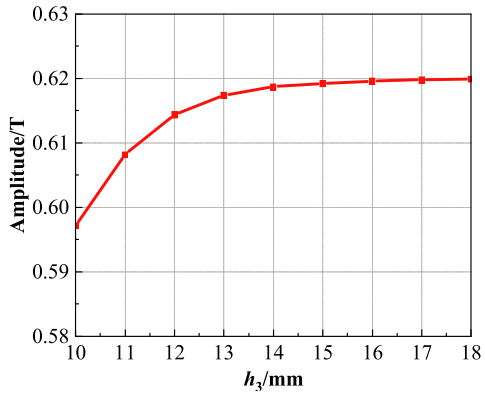

FIGURE 6. Curve of mean fundamental amplitude of air gap magnetic flux density with h_3 variatio.

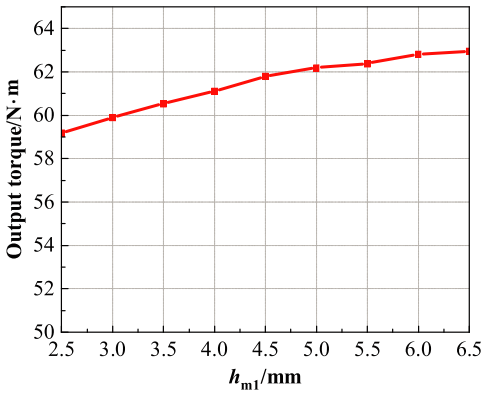

FIGURE 7. Percentage diagram of torque ripple effect with h_{m1} variation.

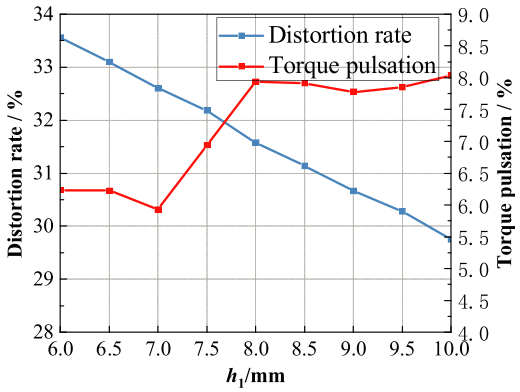

FIGURE 8. Curves of distortion rate and torque ripple changing with h_1.

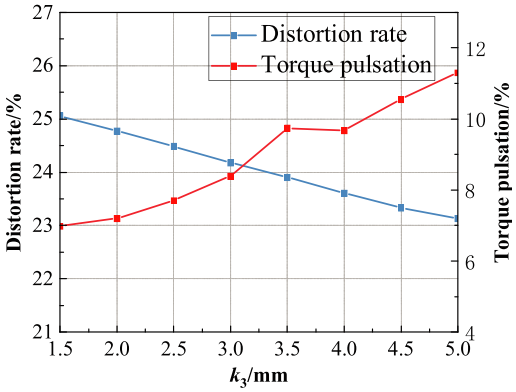

FIGURE 9. Curves of distortion rate and torque ripple with k_3.

larger than 5 mm. The permanent magnet reluctance increases when h_{m1} is larger than 5 mm, so h_{m1} is chosen to be 6 mm.

When $h_3 = 15$ mm, $h_{m1} = 6$ mm, the finite element analysis of h_1, distortion rate and torque pulsation with h_1 change curve are shown in Figure 8. As can be seen from Figure 8, with the increase of h_1, the overall aberration rate shows a gently decreasing trend, and the curve is close to a linear relationship; the torque pulsation fluctuates and decreases in the interval of $h_1 = 6 \sim 7$ mm, increases sharply in the interval of $7 \sim 8$ mm, and decreases and then rises in the interval of $8 \sim 10$ mm. Since the smaller distortion rate and torque pulsation are more favorable to the improvement of HESG performance, and the change of distortion rate in the graph is larger than the change of torque pulsation, $h_1 = 9$ mm is selected.

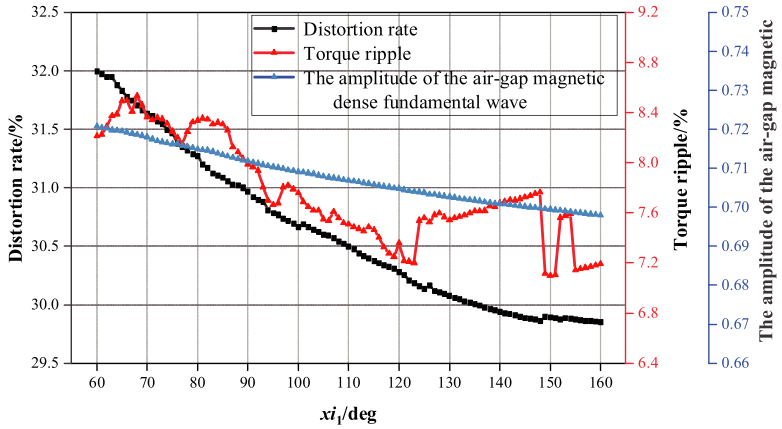

FIGURE 10. Graph of the variation of the fundamental amplitude of air gap magnetic flux density, distortion rate, and torque ripple with respect to xi_1.

At $h_3 = 15\,\text{mm}$, $h_{m1} = 6\,\text{mm}$, $h_1 = 9\,\text{mm}$, the finite element analysis of k_3, distortion rate and torque pulsation with k_3 change curves are shown in Figure 9. As can be seen from Figure 9, with the increase of k_3, the overall aberration rate shows a gently decreasing trend, and the curve is close to a linear relationship. When k_3 is $1 \sim 3.5\,\text{mm}$, torque pulsation increases gradually, and the slope the curve of torque pulsation increases gradually. When k_3 is $3.5 \sim 5\,\text{mm}$, the torque pulsation fluctuates and rises in the interval, and the aberration rate change in the Figure is smaller than the change of the torque pulsation; k_3 is selected as 2 mm.

The finite element analysis of xi_1 at $h_3 = 15\,\text{mm}$, $h_{m1} = 6\,\text{mm}$, $h_1 = 9\,\text{mm}$, and $k_3 = 2\,\text{mm}$ yields the air-gap magnetically dense fundamental wave amplitude, aberration rate, and torque pulsation versus xi_1 as shown in Figure 10.

As can be seen from Figure 10, the distortion rate gradually decreases with the increase of xi_1, but the rate of decrease decreases continuously. When xi_1 is smaller than 123°, the torque pulsation value fluctuates with the increase of xi_1, but with overall decreasing trend; when xi_1 is $123 \sim 148°$, the torque pulsation value shows an overall increasing trend; when xi_1 is larger than 148°, the torque pulsation value shows a drastic fluctuation. With the increase of xi_1, the air-gap magnetic density fundamental wave amplitude shows a gentle decrease. In order to make the electro-excitation magnetic circuit have a certain space, it is recommended that the angle is less than 130°. According to analyzing the trend of the three quantitative indicators, this paper selects $xi_1 = 119°$ which is more appropriate. At this time, the value of torque pulsation is 7.25%; the air-gap magnetomagnetic density fundamental wave amplitude is 0.705 T; the distortion rate is 30.37%.

3.2. Optimization of Rotor Parameter Impact Analysis Based on Taguchi's Method

According to the above main influencing factors and quantitative objectives, the maximum output torque, torque pulsation, air-gap magneto-density fundamental waveform amplitude, and air-gap magneto-density waveform aberration rate are selected as the optimization objectives, and b_{m1}, b_{m2}, k_1, k_2, and h_5 are selected as the optimization factors, where five influencing levels are selected isometrically, and the table of the optimization factor levels is shown in Table 2.

TABLE 2. HESG rotor optimization parameters and factor level experimental table.

Parametric	Level 1	Level 2	Level 3	Level 4	Level 5
b_{m1}/mm	8	9	10	11	12
k_1/mm	18	19	20	21	22
b_{m2}/mm	4	6	8	10	12
h_5/mm	6	7	8	9	10
k_2/mm	3	4	5	6	7

According to the orthogonal experimental table and Taguchi's algorithm, the orthogonal array is obtained. Finite element simulations are conducted on the orthogonal array experimental design, and the data are processed to obtain the experimental matrix and finite element analysis results, as shown in Table 3.

In order to analyzes the effect of parameter variations in the optimization factors of the starter generator rotor on the four optimization objectives, the analysis was carried out by calculating the average values based on the results obtained from the tests. The average value is calculated by the formula:

$$M(s) = \frac{1}{n_s}\sum_{i}^{n_s} S_i = \frac{1}{25}\sum_{i=1}^{25} S(i) \tag{9}$$

where n_s is the number of experiments; i is a constant of the minimum value of the output torque of the starter generator, $i = 1, 2, 3 \ldots n_s$; S_i is the average of the objectives of the first trial. The average values of the results obtained from the tests were calculated as shown in Table 4.

The average value of performance indicators at different factor levels can be calculated as:

$$M_{xi} = \frac{1}{4}\left[M_x(u_i) + M_x(v_i) + M_x(w_i) + M_x(n_i)\right] \tag{10}$$

TABLE 3. Experimental matrix and finite element analysis results.

Number of times	Experimental Matrix					T_{max}/N m	K_T/%	G_{Bg}/T	*THD*/%
	b_{m1}/mm	k_1/mm	b_{m2}/mm	h_5/mm	k_2/mm				
1	1	1	1	1	1	55.5	7.3	0.7	18.2
2	1	2	2	2	2	62.2	9.2	0.7	19.5
3	1	3	3	3	3	66.6	8.6	0.7	25.6
4	1	4	4	4	4	66.7	4.5	0.8	32.5
5	1	5	5	5	5	60.4	4.5	0.7	29.6
6	2	1	2	3	4	66.3	9.8	0.7	19.7
7	2	2	3	4	5	69.1	5.5	0.8	27.5
8	2	3	4	5	1	70.0	10.4	0.8	20.6
9	2	4	5	1	2	73.8	6.8	0.8	28.2
10	2	5	1	2	3	68.9	5.6	0.8	32.8
11	3	1	3	5	2	65.1	9.5	0.8	15.6
12	3	2	4	1	3	73.8	11.3	0.8	18.2
13	3	3	5	2	4	75.8	7.3	0.8	25.9
14	3	4	1	3	5	70.4	6.6	0.8	30.1
15	3	5	2	4	1	74.0	11.5	0.8	21.3
16	4	1	4	2	5	74.8	9.6	0.8	17.3
17	4	2	5	3	1	70.3	9.3	0.8	13.9
18	4	3	1	4	2	74.7	12.4	0.8	15.6
19	4	4	2	5	3	76.8	7.9	0.8	23.8
20	4	5	3	1	4	76.5	7.6	0.8	27.8
21	5	1	5	4	3	69.7	7.3	0.8	12.0
22	5	2	1	5	4	76.5	9.5	0.8	17.0
23	5	3	2	1	5	78.3	7.5	0.9	23.4
24	5	4	3	2	1	79.1	12.6	0.9	13.8
25	5	5	4	3	2	82.8	8.6	0.9	21.2

TABLE 4. Average performance indicator values.

Parametric	T_{max}/N m	K_T/%	G_{Bg}/T	THD/%
$\bar{m}$	71.12	8.43	0.79	22.03

where M_{xi} is the average value of the performance index under the ith optimization factor of the parameter; M_x is the performance index of the parameter under a particular experiment; u_i, v_i, w_i, n_i is the experimental sequence number.

According to formula (6), curves showing the variations of output torque, torque ripple, fundamental amplitude of air-gap magnetic flux density, and distortion rate with respect to the levels of each optimization factor are as shown in Figure 11, and then according to the change of each parameter to its variance as a percentage of the analysis, the analysis of the data is shown in Table 5, with the combination of the two to derive the results of the optimization of the variance of the calculation formula:

$$S(s) = \frac{1}{5}\sum_{i=1}^{5}[M_{xi} - M(s)]^2 \tag{11}$$

where S is the individual performance indicators; $S(s)$ is the variance of a performance indicator under parameter S; $M(s)$ is the total mean of a performance indicator.

According to Figure 11 and Table 5, the influences of each optimization factor on the output torque and air-gap magnetic density fundamental waveform amplitude are very similar, so the four objectives are reorganized into three objectives, namely, output torque, torque pulsation, and aberration rate. b_{m1} accounts for more than 70% of the variance of the influence on the output torque and air-gap magnetic density fundamental waveform amplitude, close to 30% for the influence on torque pulsation and aberration rate. The main influence of output torque can be approximated as b_{m1}, and part of the influence of torque pulsation and distortion rate is also b_{m1}. Similarly, it can be considered that k_2 has an important influence on the torque pulsation, and k_1 has an important influence on the distortion rate. In conclusion, b_{m2}, h_5, and b_{m2} can be optimized first, and then k_1 and k_2 can be simulated directly.

According to Figure 11, with the increase of h_5, the output torque and distortion rate are gradually reduced; from Table 5, the variance of the influence of h_5 on the output torque, torque pulsation, and distortion rate is close to the ratio. Consider selecting $h_5 = 9$ mm. With the increase of b_{m2}, the output torque firstly increases and then decreases; the distortion firstly decreases and then stabilizes; the influence of b_{m2} on the torque pulsation is much higher than that on the output torque and distortion rate. Consider selecting $b_{m2} = 10$ mm

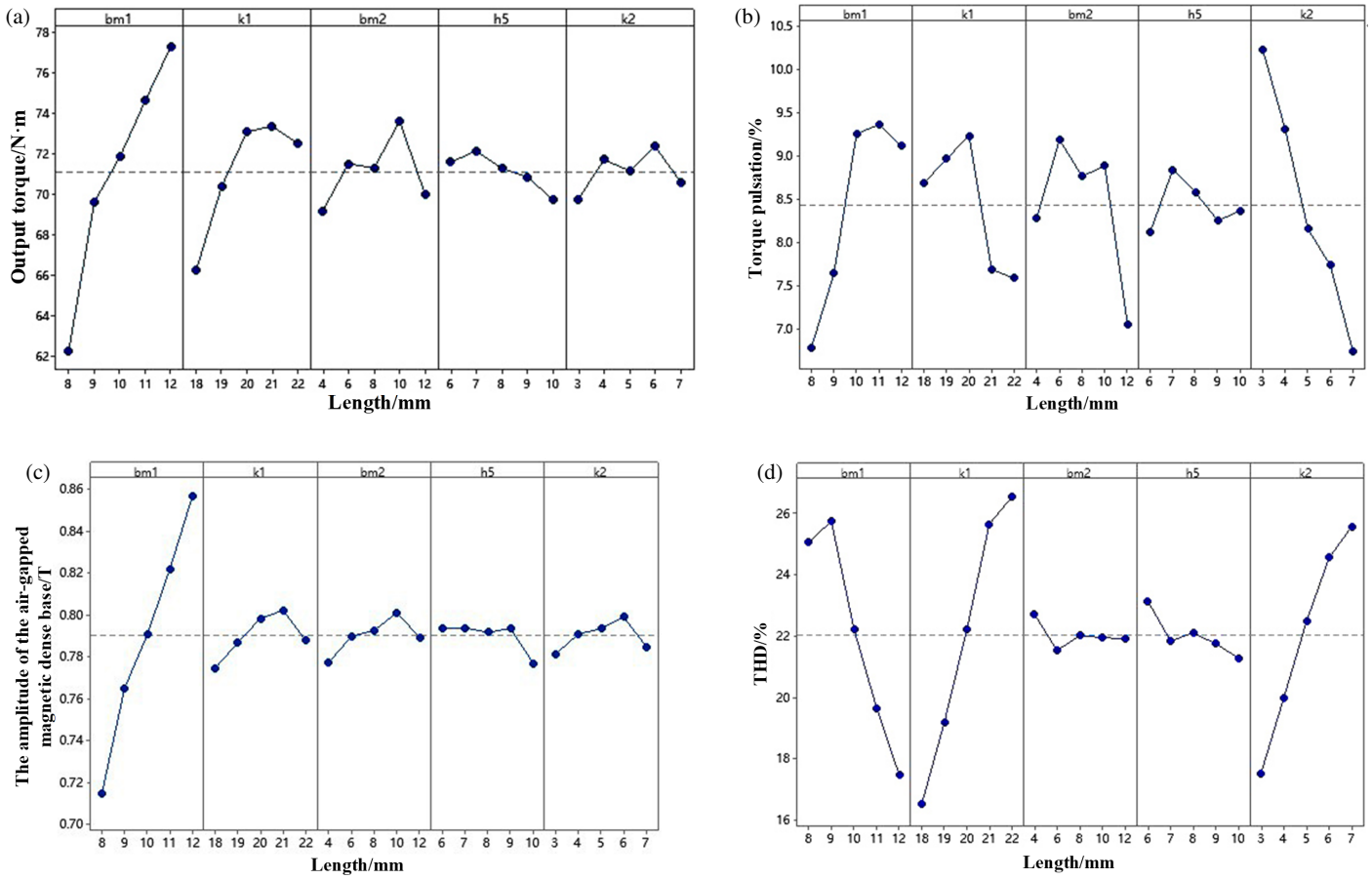

FIGURE 11. (a) The influence of each optimization factor on the output torque. (b) The influence curve of each optimization factor on torque ripple. (c) The influence curve of each optimization factor on the amplitude of air gap fundamental wave. (d) Influence graph of each optimization factor on distortion rate.

TABLE 5. Table of the percentage of variance of each optimization factors.

Parametric	$T_{\max}$		K_T		G_{Bg}		THD	
	Variance (statistics)	Specific gravity %	Variance (statistics)	Specific gravity %	Variance (statistics)	Specific gravity %	Variance (statistics)	Specific gravity %
b_{m1}	26.21	71.12	1.07	29.42	0.00235	90.89	9.91	29.66
k_1	6.98	18.94	0.45	12.46	0.00009	3.67	14.29	42.73
b_{m2}	2.24	6.09	0.56	15.57	0.00006	2.28	0.15	0.45
h_5	0.66	1.78	0.64	1.76	0.00004	1.66	0.38	1.44
k_2	0.76	2.07	1.48	40.79	0.00004	1.5	8.7	26.02
(grand) total	36.85	100	3.6	100	0.00258	100	33.43	100

with the increase of b_{m1}. The output torque increases rapidly; the torque pulsation firstly increases and then fluctuates to decrease; the distortion rate decreases rapidly. Due to the high requirement of output torque when starting the starter generator and the space requirement of the magnetic circuit for electric excitation, $b_{m1} = 12$ mm is selected.

The finite element simulation of k_1 and k_2 is carried out, and the surface plots of output torque, torque pulsation, and distortion rate with k_1 and k_2 are shown in Figure 12 according to the simulation data.

According to Figure 12(a), the output torque has higher values in the region where k_1 is $19.5 \sim 21$ mm; k_2 is $4 \sim 7$ mm; the output torque increases with the increase of k_1. According to Figure 12(b), the torque pulsation has lower values in the region where k_2 is $5 \sim 8$ mm. According to Figure 12(c), it can be seen that the aberration rate has a lower value in the region where k_2 is $3 \sim 6$ mm. According to Figure 12(c), it can be seen that the aberration rate has a lower value in the region where k_2 is $3 \sim 6$ mm, but with the increase of k_1, the region of low value of aberration rate is shifted to the smaller part of

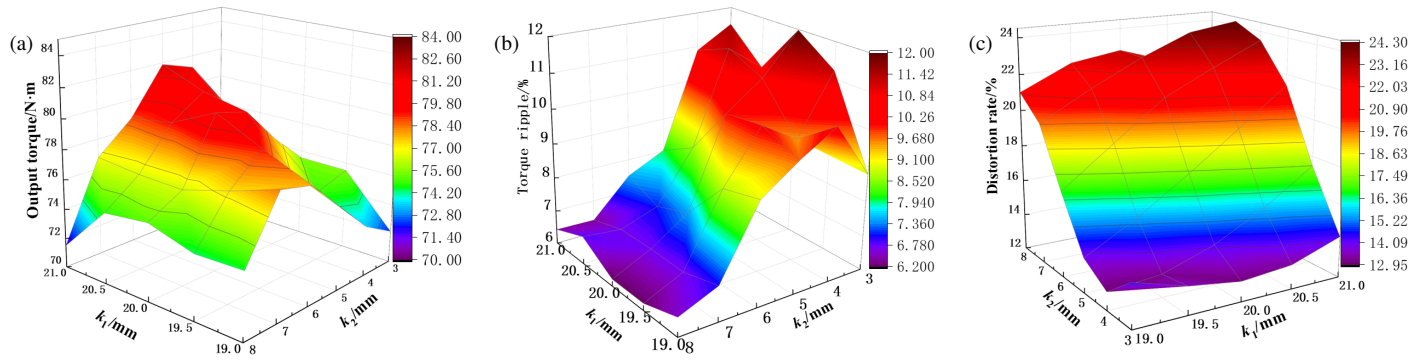

FIGURE 12. (a) Output torque changes with k_1 and k_2. (b) Curved diagram of the change of torque pulsation with k_1 and k_2. (c) Change of distortion rate with k_1 and k_2.

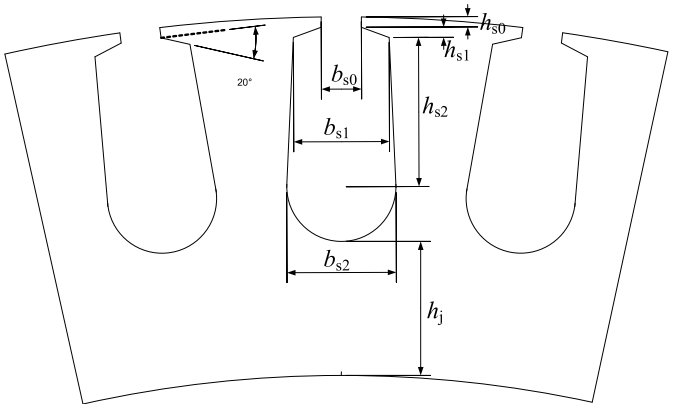

FIGURE 13. Schematic diagram of related dimensions of stator slot.

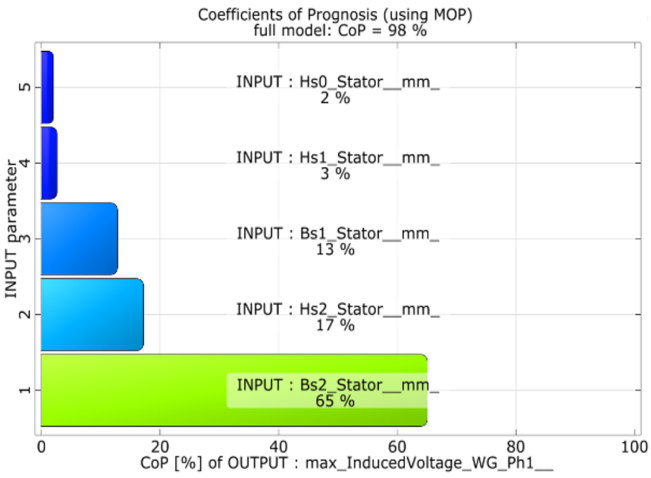

FIGURE 14. Ratio chart of predictive model variables.

the value of k_2. In summary, $k_1 = 20.5$ mm and $k_2 = 5.5$ mm.

3.3. Stator Slot Dimensions

In order to ensure the high stability of the output performance of the HESG with convex pole electromagnetic and permanent magnet composite poles and to improve the performance of the starter generator, a sample of design experiment is conducted

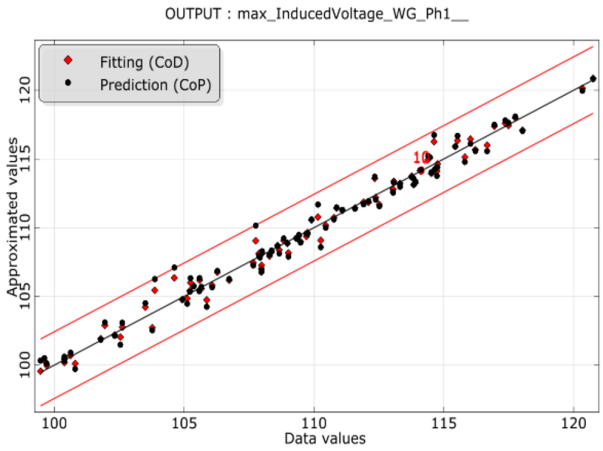

FIGURE 15. Residual graph.

using the space-filling Latin hypercube experimental design method. The experimental design variables are stator slot parameters b_{s0}, b_{s1}, b_{s2}, h_{s0}, h_{s1}, h_{s2}, which are continuous variables, and the number of sample points is 100. The schematic diagram of stator related parameters is shown in Figure 13.

Stator slot opening width is b_{s0}, stator slot opening height h_{s0}, stator slot bottom width b_{s2}, stator slot top bottom width b_{s1}, stator slot sloping shoulder height h_{s1}, and stator yoke height h_j.

To ensure the filling rate of the slots, constraints need to be imposed on the size of the stator slots. The design space constraint inequality is:

$$\begin{cases} 1.5 \le b_{s0} \le 3 \\ 5 \le b_{s1} \le 8 \\ 5 \le b_{s2} \le 7.5 \\ 0.5 \le h_{s0} \le 2 \\ 0.5 \le h_{s1} \le 2 \\ 13 \le h_{s2} \le 17 \\ b_{s0}h_{s0} + \frac{(b_{s0}+b_{s1})h_{s1}}{2} + \frac{(b_{s2}+b_{s1})h_{s2}}{2} + \frac{\pi b_{s2}^2}{8} \ge 109 \end{cases} \tag{12}$$

For the parameter data of the sample point design, finite element simulation is carried out, and the prediction model is evaluated using the software's assessment of the prediction model's

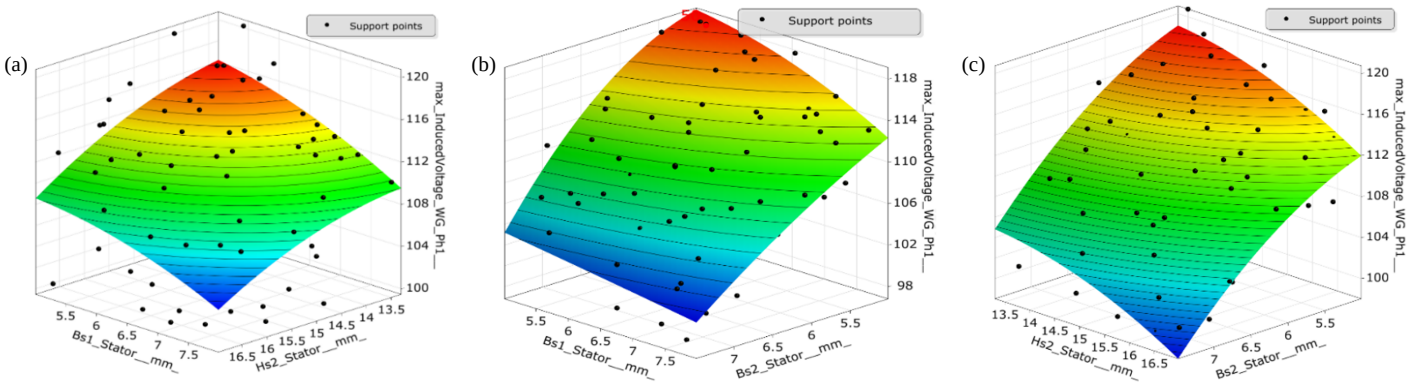

FIGURE 16. (a) The surface diagram of the induced electromotive force is fitted with the change of b_{s1} and h_{s2}. (b) The surface diagram of the induced EMF is fitted with the change of b_{s1} and b_{s2}. (c) The surface diagram of the induced EMF is fitted with the change of h_{s2} and b_{s2}.

quality indicator, the Coefficient of Prediction [18]. The plot of the proportion of its variables in the prediction model with the residuals is shown below.

According to Figure 14, the target prediction coefficient COP of the model is 0.98, which is very close to 1, indicating that the model is established effectively, and its variables b_{s0}, b_{s1}, b_{s2}, h_{s0}, h_{s1}, h_{s2} are in the ratios of 0%, 13%, 65%, 2%, 3%, and 17%, respectively. Among them, the proportions of b_{s2}, h_{s2}, and b_{s1} are relatively large. Therefore, the main influencing factors are b_{s2}, h_{s2}, and b_{s1}. According to Figure 15, it can be seen that according to the predictive model function most of the sample points are related to the model, so the model function is built to hold. The three main factors are intersected to analyze the effect on the induced electromotive force (EMF), and the fitted surface diagrams of the induced electromotive force with the variation of b_{s1} and h_{s2}, the fitted surface diagram of the induced electromotive force with the variation of b_{s1} and b_{s2}, and the fitted surface diagram of the induced electromotive force with the variation of h_{s2} and b_{s2} are shown in Figure 16.

According to Figure 16(a), the induced electromotive force decreases gradually with the increase of h_{s2} and b_{s1}, and there is a large value of induced electromotive force when h_{s2} and b_{s1} take smaller values. According to Figure 16(b), the induced electromotive force decreases with the increase of b_{s1}, b_{s2}, and has a larger value when b_{s2} and b_{s1} take smaller values. According to Figure 16(c), the induced electromotive force decreases with the increase of h_{s2} and b_{s2}, and has a larger value when h_{s2} and b_{s2} take smaller values. The induced electromotive force amplitude of the fitted surface plot containing the variable b_{s2} among the three variables varies a lot, which is consistent with the fact that the variable b_{s2} has the highest value in the model share before.

The peak cogging torque of the starter generator is introduced into the objective optimization, and the requirement of the starter generator to take the maximum value of the induced electromotive force as well as the cogging torque to take the smaller value is analyzed using the Pareto principle. The Pareto diagram is shown in Figure 17.

The Pareto front curve is shown as the red line in Figure 17, and the points on the red line are the peak cogging torque or the parameter points with larger values of the induced electromotive force (EMF). In this case, the A-phase induced electromotive force is larger; the cogging torque peak value is smaller; the stator slot area meets the slot fullness requirement.

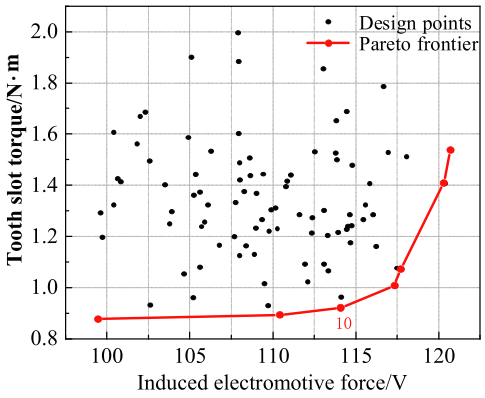

FIGURE 17. Pareto front chart.

4. BEFORE AND AFTER OPTIMIZATION ANALYSIS

The simulation model is established by using the optimized parameters. The comparison chart of the magnetic density amplitude of the air gap before and after optimization, the comparison chart of the corresponding electromotive force curve, the output voltage change curve of the HESG at the same speed, and the power characteristic curve of the starter generator under different load currents are shown in Figure 18.

From Figures 18(a) and 18(b), it can be seen that the optimized air-gap magneto-density fundamental waveform amplitude is improved from 0.81 T to 0.87 T, which is 7.4% higher; the 5th harmonic is significantly reduced; the output performance of the HESG is improved; the induced electromotive force (EMF) amplitude is improved from 112.6 V to 114.3 V, which is 1.5% higher; the curvature of curves at the two sides of the peaks of the optimized waveforms decreases. By calculating the aberration rate of the air-gap magneto-density waveforms, it can be seen that the distortion rate is reduced by 10.6% from 28.4% to 25.4%, and the overall smoothness of the waveform is improved, which can improve the output quality of the designed HESG.

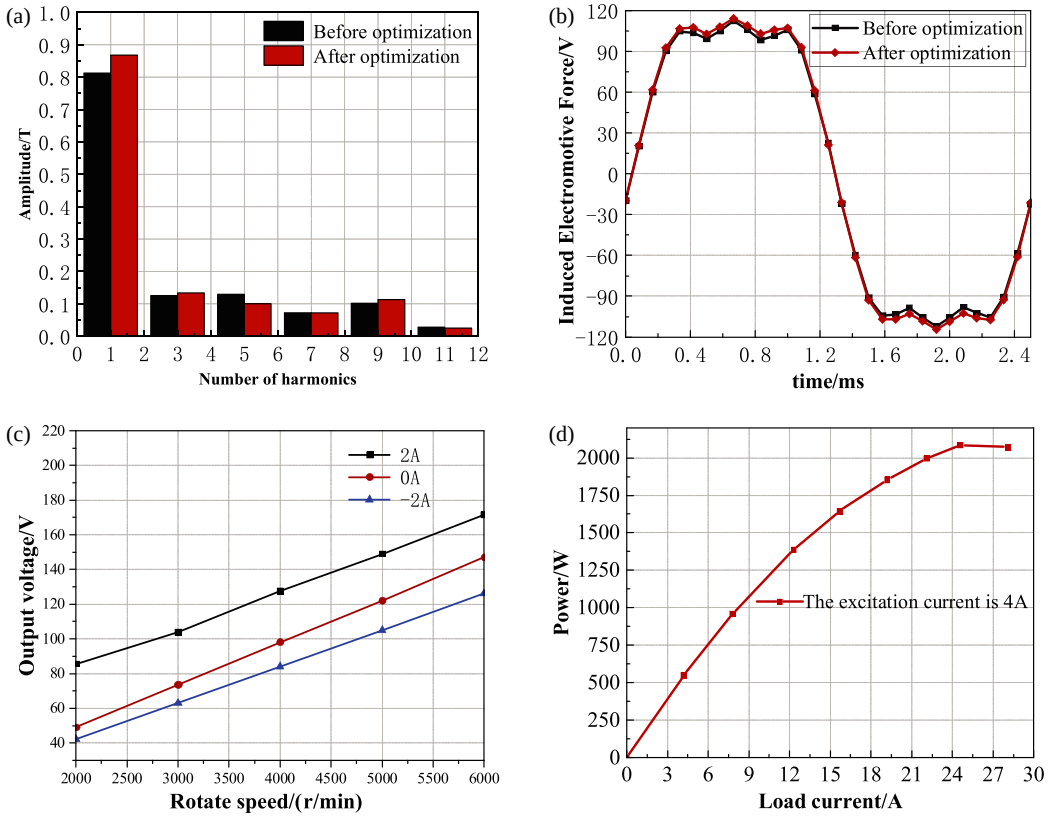

FIGURE 18. (a) Comparison chart of the average air gap magnetic density amplitude before and after optimization. (b) Optimized the comparison chart of the front and rear induced EMF curves. (c) Output voltage change curve of mixed excitation starter generator at different speeds. (d) Power characteristic curves of starting generators under different load currents.

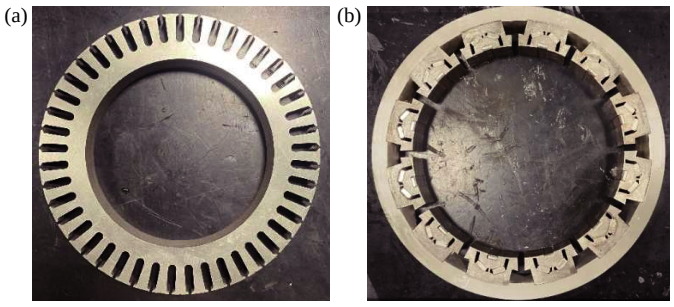

FIGURE 19. (a) Internal stator. (b) External rotor.

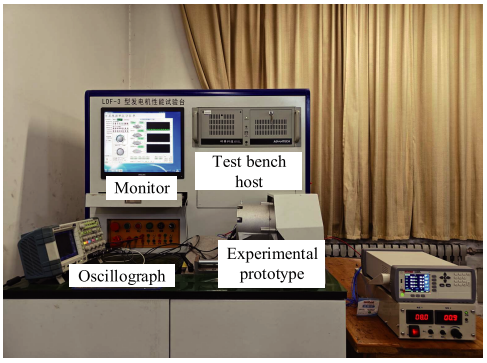

FIGURE 20. Generator performance test platform.

From Figures 18(c) and 18(d), it can be seen that the output voltage of HESG increases with the increase of rotational speed, when the rotational speed is unchanged; the output voltage increases with the increase of excitation current, when the starter generator is at the rated rotational speed; the excitation current is increased from 0 A to 2 A; the output voltage is increased from 98.1 V to 127.68 V, which is a larger increase; when the rotational speed is lower, the starter generator can still keep the output. The voltage is kept above 84 V, which shows that the starter generator has a stronger magnetizing ability and a wider voltage regulation range. When the load becomes bigger, the output power of HESG becomes bigger, but when the load is too big, the output power will decrease instead, and increasing the excitation current can effectively slow down this trend, which can make the starter generator output higher power under bigger load.

5. EXPERIMENTAL VALIDATION

According to the optimized parameters, the prototype is fabricated, the experimental platform built, and the prototype experiment carried out. The structure of HESG stator-rotor is shown in Figures 19(a) and 19(b), and the HESG experimental platform is shown in Figure 20.

After the test data of the prototype is outputted by the processor, the data points are extracted and compared with the theoretical values, and the torque governing characteristic curve and

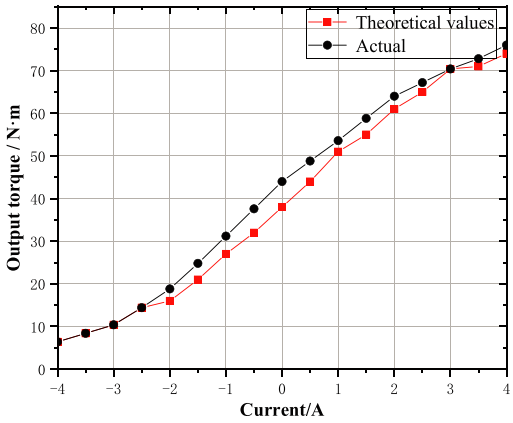

FIGURE 21. Comparison of the torque output characteristics curves with different excitation currents.

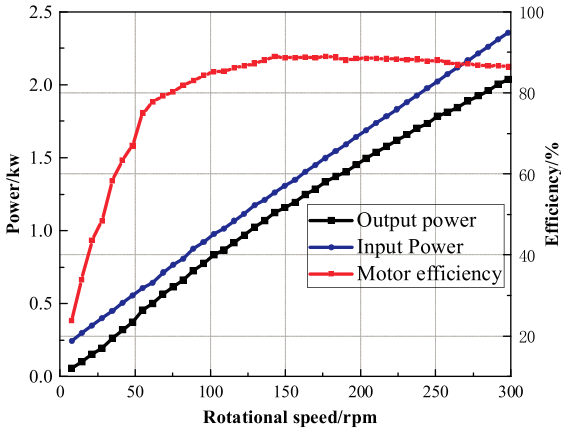

FIGURE 22. Power characteristic curve.

power characteristic curve under different excitation currents at 200 r/min are shown in Figures 21 and 22.

It can be seen from Figure 21 that there is a certain discrepancy between the experimental and simulated values, which is due to differences in processing techniques; however, their waveform trends are the same, and the error values fall within the acceptable range, which validates the accuracy of the finite element analysis. As can be seen in Figure 22, the output power grows approximately linearly with the increase of rotational speed, and when the rotational speed reaches 300 rpm, the output power reaches 2.0 KW. At this time, the output power reaches the maximum value of the hair state. Input power also rises with the rise in speed, at 300 rpm when the input power reaches a maximum value of 2.2 KW. When the rotational speed is lower than 60 rpm, the HESG efficiency rises rapidly. When the rotational speed exceeds 60 rpm, the trend of efficiency improvement slows down. When the rotational speed is 300 rpm, the efficiency is close to 90%. This is a relatively high efficiency state that can be achieved under constant rotational speed conditions.

6. CONCLUSION

In this paper, a new type of salient pole electromagnetic and permanent magnet composite pole HESG topology is proposed, which uses hierarchical optimization to quickly screen the main influencing parameters of the magnetic field, reduces the workload of finite element analysis, combines the Taguchi method and finite element simulation to optimize the rotor parameters with multiple objectives, and uses the response surface method to analyze and optimize the influence of stator slot size on the HESG performance. Simulation and experiments show that the fundamental amplitude of the air-gap magnetic density is increased by 7.4%; the distortion rate is reduced by 10.6%; the output voltage is increased to 127.68 V; the output performance and magnetic modulation ability are significantly improved, which verifies the effectiveness of the structure and the feasibility of the analysis method. The hierarchical optimization method used in this paper fully considers the different influences of different parameters on HESG performance and provides certain theoretical reference for the structural modeling and magnetic field analysis of HESGs with complex structures. In addition, this method can quickly screen the influencing parameters of the main magnetic field and can be combined with finite element method to be applied to the optimization analysis of HESG, which has certain theoretical and practical significance for the design and electromagnetic performance analysis of high-performance and complex-structure HESGs.

REFERENCES

[1] Zhang, X. Y., Q. J. Du, S. L. Ma, *et al.*, "Development of hybrid excitation generator for automobiles," *Automotive Engineering*, Vol. 39, No. 7, 822–826, 2017.

[2] Dai, J., "Research on tangential structure permanent magnet synchronous motor and its hybrid excitation technology," Ph.D. dissertation, Nanjing University of Aeronautics and Astronautics, Nanjing, China, 2015.

[3] Geng, H., X. Zhang, Y. Zhang, W. Hu, Y. Lei, X. Xu, A. Wang, S. Wang, and L. Shi, "Development of brushless claw pole electrical excitation and combined permanent magnet hybrid excitation generator for vehicles," *Energies*, Vol. 13, No. 18, 4723, 2020.

[4] Fathollahi-Fard, A. M. and M. Hajiaghaei-Keshteli, "A stochastic multi-objective model for a closed-loop supply chain with environmental considerations," *Applied Soft Computing*, Vol. 69, 232–249, 2018.

[5] Farahani, E. F., M. A. J. Kondelaji, and M. Mirsalim, "An innovative hybrid-excited multi-tooth switched reluctance motor for torque enhancement," *IEEE Transactions on Industrial Electronics*, Vol. 68, No. 2, 982–992, 2021.

[6] Tounsi, S., "Constrained design and control of trapezoidal waves-forms hybrid excitation synchronous motor increasing energy accumulator lifetime," *International Transactions on Electrical Energy Systems*, Vol. 29, No. 12, e12127, 2019.

[7] Ning, B., C. H. Zhao, and G. Liu, "Technical status and new progress of hybrid excitation motor," *Motor and Control Applications*, Vol. 44, No. 5, 1–12, 2017.

[8] Quan, X. W., "Design analysis and optimization of dual-rotor hybrid excitation axial flux-switching permanent magnet motor," Ph.D. dissertation, Xi'an University of Technology, Xi'an, China, 2020.

[9] Li, W. Y., S. R. Huang, and Q. Zhang, "Multi-domain simulation analysis of hybrid excitation claw-pole belt starter generator for hybrid vehicles," *Chinese Journal of Electrical Engineering*,

Vol. 30, No. 36, 7–15, 2010.

[10] Zhang, C., "Design and performance calculation of hybrid excitation synchronous generator," Ph.D. dissertation, Nanchang University, Nanchang, China, 2019.

[11] Dai, J., Z. Zhang, Y. Mu, *et al.*, "Characterization of armature reactive magnetic field and inductance of rotor magnetic split hybrid excitation synchronous motor," *Journal of Electro Technology*, Vol. 30, No. 12, 276–283, 2015.

[12] Zhang, X. X., "Optimized design and research of rotor magnetic split hybrid excitation drive motor," Ph.D. dissertation, Nanjing University of Aeronautics and Astronautics, Nanjing, China, 2017.

[13] Wang, C., Z. R. Zhang, and Y. Liu, "Optimization of rotor eddy current loss and heat dissipation in high torque density rotor magnetic split hybrid excitation motor," *Chinese Journal of Electrical Engineering*, Vol. 41, No. 21, 7476–7486, 2021.

[14] Ali, H., E. Sulaiman, M. Jenal, F. Amin, I. Ali, *et al.*, "Design improvement and comparison of hybrid excitation FSM using segmental rotor," in *2019 IEEE 15th International Colloquium on Signal Processing & Its Applications (CSPA)*, 186–191, Penang, Malaysia, 2019.

[15] Nedjar, B., S. Hlioui, M. Lécrivain, Y. Amara, L. Vido, and M. Gabsi, "Study of a new hybrid excitation synchronous machine," in *2012 XXth International Conference on Electrical Machines*, 2927–2932, Marseille, France, 2012.

[16] Finken, T. and K. Hameyer, "Study of hybrid excited synchronous alternators for automotive applications using coupled FE and circuit simulations," *IEEE Transactions on Magnetics*, Vol. 44, No. 6, 1598–1601, 2008.

[17] Wardach, M., P. Paplicki, and R. Palka, "A hybrid excited machine with flux barriers and magnetic bridges," *Energies*, Vol. 11, No. 3, 676, 2018.

[18] Park, J. M., S. I. Kim, J. P. Hong, and J. H. Lee, "Rotor design on torque ripple reduction for a synchronous reluctance motor with concentrated winding using response surface methodology," *IEEE Transactions on Magnetics*, Vol. 42, No. 10, 3479–3481, 2006.

Erratum to "Magnetic Density Analysis and Performance Optimization of Hybrid Excitation Starter Generator"

by Hui Zhu, Wenjing Hu, Wei Wang, Shiqiang Liu, Xia Zhang, Jiewen Li, and Xingxu Jin
in *Progress in Electromagnetic Research C*, Vol. 159, 169–181, 2025

The original affiliation for the first author, Hui Zhu, was incorrectly listed as:

"School of Engineering, Shandong Union University, China"

The correct affiliation for the first author, Hui Zhu, should be:

"School of Engineering Science, Shandong Xiehe University, Jinan 250107, China"

Received 8 December 2025, Added 9 December 2025